https://doi.org/10.5194/tc-2023-30
Preprint. Discussion started: 2 March 2023
© Author(s) 2023. CC BY 4.0 License.

The Cryosphere Discussions

Microstructure-based modelling of snow mechanics: experimental evaluation on the cone penetration test

Clémence Herny[1,2], Pascal Hagenmuller[1], Guillaume Chambon[2], Isabel Peinke[1], Jacques Roulle[1]

[1]Univ. Grenoble Alpes, Univ. de Toulouse, Météo-France, CNRS, CNRM, Centre d'Etude de la Neige, Grenoble, Franc
[2]Univ. Grenoble Alpes, CNRS, INRAE, IRD, Grenoble INP, IGE, Grenoble, France

Correspondence to: Clémence Herny (clemence.herny@gmail.com)

Abstract. Snow is a complex porous material presenting various microstructural patterns. This microstructure controls the mechanical properties of snow, and this control still needs to be better understood. Recent numerical developments based on three-dimensional tomographic data have provided new insights into snow mechanical behaviour. In particular, the discrete element method combined with the snow microstructure captured by tomography and the mechanical properties of ice has been used to reproduce the brittle properties of snow. However, these developments lack experimental evaluation so far. In this study, we evaluate a numerical model based on the discrete element method with cone penetration tests on centimetric samples. This test is commonly used to characterise the snowpack stratigraphy but also brings into play complex mechanical processes and deformation patterns. We measured the snow microstructure on different samples before and after a cone penetration test with X-ray tomography. The cone test was conducted with the Snow MicroPenetrometer (5 mm cone diameter), which recorded the force profile at high resolution. The initial microstructure and the ice properties fed the model, which can reproduce the exact same test numerically. We evaluated the model on the measured force profile and the displacement field derived from the difference between the initial and final microstructures. The model reasonably reproduced the force profiles in terms of average force, force standard deviation, and the correlation length of the force fluctuations. When the contact law describing ice mechanics is adjusted in the range of reasonable values for ice, the agreement becomes good on all three parameters. The model also well reproduced the measured deformation around the cone tip, which is less sensitive to the contact law parameterization. Overall, the model is capable of distinguishing the different microstructural patterns tested. Therefore this confrontation of numerical results with experimental measurements for this configuration gives confidence in the reliability of the numerical modelling strategy. The model could be further applied with different boundary conditions and used to characterise the mechanical behaviour of the snow better.

1 Introduction

Snow is a brittle and porous material existing on Earth close to its melting point. The thermodynamical conditions in the clouds govern the snowflake morphology and, once deposited on the ground, snow continues to evolve via metamorphism. The snow material is thus characterised by a large variety of microstructural patterns (grain size, grain shape, density) classified into

https://doi.org/10.5194/tc-2023-30
Preprint. Discussion started: 2 March 2023
© Author(s) 2023. CC BY 4.0 License.


different snow types (Fierz et al., 2009). It has been established that the snow microstructure controls the properties of snow (Shapiro et al., 1997; Johnson and Schneebeli, 1999; Schneebeli, 2004). For instance, weak layers involved in avalanche triggering (Schweizer et al., 2003) are usually constituted of specific snow types (depth hoar, surface hoar, precipitation particle, faceted crystals) characterised by low cohesion and low strength (Jamieson and Johnston, 1992). The link between the snow microstructure and its properties, especially its mechanical properties, is still not well understood, even it is crucial for many applications, such as for avalanche forecasting (Schweizer et al., 2003, Jamieson and Johnston, 1992), snowpack modelling (Calonne et al. 2014), ice core interpretation (Montagnat et al. 2020) or geotechnics (Shapiro et al., 1997). In particular, the brittle failure occurring at high shear rate ($> 10^{-4}$ s^{-1}) during the release of an avalanche remains represented by very coarse empirical laws (Brun et al., 1992; Bartelt, et al. 2002; Vionnet et al. 2012) and lacks of relevant microstructural proxies (Shapiro et al., 1997). In this elastic-brittle regime (rapid and large deformations), the mechanical behaviour of snow is mainly controlled by bond failure and grain rearrangements (Narita, 1983).

The snow microstructure and its evolution can be captured at high resolution (tens of microns) with X-ray micro tomography imaging (µCT) (Coléou et al., 2001; Freitag et al., 2004; Schneebeli, 2004; Heggli et al., 2011). This non-destructive method preserves the snow microstructure and resolves the shape of snow grains, grain bonds and porosity which is of primary importance for mechanical studies. In particular structural properties of snow, such as density, specific surface area (SSA), correlation length, bond characteristics, can be evaluated from tomographic data (e.g. Schneebeli, 2004; Schneebeli et al., 2004; Hagenmuller et al., 2014a; Calonne et al., 2014; Proksch et al., 2015). The tomographic data are also used as a basis for numerical modelling (Schneebeli, 2004; Schneebeli et al., 2004; Hagenmuller et al., 2015) or calibration/validation data of statistical empirical models retrieving physical and mechanical properties from other measurements (e.g. Proksch et al., 2015; Reuter et al., 2019). However, this method is time-expensive and not adapted to routine measurements in the field.

An objective and relatively easy-to-set-up method to measure the mechanical properties of snow is the Cone Penetration Test (CPT). This method has been widely used to characterise soil stratigraphy (Lunne et al., 1997) and adapted to snowpack stratigraphy (Gubler, 1975; Schaap and Fohn, 1987; Dowd and Brown, 1986; Schneebeli and Johnson, 1998; Mackenzie and Payten, 2002; McCallum, 2014). The CPT provides a force profile by measuring the resisting force exerted on a tip penetrating, at a constant rate, into a material. The development of high-resolution digital penetrometers dedicated to snow studies (Schneebeli and Johnson, 1998; Mackenzie and Payten, 2002; McCallum, 2014) have provided the possibility to resolve the force profile at a microscopic scale and capture the high-frequency fluctuations of the force signal up to a metre depth. The force penetration profile contains valuable information on the snow structural parameters at macro- and micro-scale (Löwe and van Herwijnen, 2012).

Interpretation of the CPT requires a good comprehension of the interaction between the cone tip and the snow grains and bonds. Several studies aimed to investigate the grains displacement field around the tip. Particle Image Velocimetry (PIV) imaging was performed along on snow to quantify the 2D displacement field of snow grains while the tip penetrates the snow (Floyer and Jamieson, 2010; Herwijnen, 2013; LeBaron et al., 2014). Peinke et al. (2020) developed a grain tracking algorithm

https://doi.org/10.5194/tc-2023-30
Preprint. Discussion started: 2 March 2023
© Author(s) 2023. CC BY 4.0 License.


to reconstruct from μCT the 3D displacement field of snow grains due to a CPT. All these studies revealed the development of a compaction zone (CZ) in front of the tip that cannot be neglected while interpreting force profiles.

Mechanical or statistical models have been developed to interpret the penetration signal in terms of mechanical properties. The cavity expansion model (CEM) (Bishop et al., 1945; Yu and Carter, 2002) is commonly used to interpret CPT measurements and has been applied to snow by Ruiz et al. (2016) and Peinke et al. (2020). The CEM describes the elastic-plastic deformation of the material around the tip. Macroscopic material properties can be retrieved from this model (Ruiz et al., 2016; Peinke et al., 2020). The shot noise model interprets the force signal and its fluctuations as a superposition of independent elastic–brittle ruptures occurring next to the tip (Schneebeli and Johnson, 1999; Marshall and Johnson, 2009; Löwe and van Herwijnen, 2012). The penetration process is here modelled by a Homogeneous Poisson Process (HPP) with a constant intensity (Löwe and van Herwijnen, 2012). Peinke et al. (2019) have generalised the HPP method in order to account for the transient state of the penetration process, attributed to the development of the CZ (Peinke et al., 2019). They used a Non-Homogeneous Poisson Process (NHPP) considering a depth dependency of the intensity, i.e. number of bond failures per penetration increment. Both models are based on different assumptions. First, the CEM considers snow as a continuum, while the HPP considers the discrete nature of bond failures. The continuum assumption reaches its limit for a cone diameter to mean grain ratio lower than 20 (Bolton et al. 1993), leading to a potentially erroneous interpretation of the CPT results. This configuration can be reached for CPT measurements in snow (Herwijnen, 2013; Peinke et al. 2020). Second, the force signal is influenced by the CZ (Herwijnen, 2013; LeBaron et al., 2014; Peinke et al. 2020), which is considered in the CEM approach but not in the HPP approach. This may lead to diverging estimations of the absolute value of some macroscopic snow properties (Ruiz et al., 2017). Despite the NHPP can retrieve snow microstructural properties from transient force profiles (Herwijnen, 2013; Peinke et al., 2019), the interpretation of the force profiles, resulting of independent contributions of elastic-brittle failure, neglecting the development of a CZ remains challenging (Johnson and Schneebeli, 1999; Schneebeli, 2001; Herwijnen, 2013; LeBaron et al., 2014; Ruiz et al. 2017). Therefore, none of the two methods appear to fully satisfy the specificity of snow deformation induced by CPT. Additional investigations are required to better understand the tip interaction with snow and the meaning of the derived structural proxies.

The snow properties and its strong dependence on environmental conditions make it difficult to study it experimentally (in the laboratory and in situ) in a systematic and controlled manner. Recently, numerical approaches have been developed to study the mechanical response of snow by explicitly accounting for the microstructure (Johnson and Hopkins, 2005; Gaume et al., 2015, 2017; Hagenmuller et al., 2015; Wautier et al., 2015; Mede et al. 2018b, 2020; Bobillier et al., 2020, 2021). Snow is described as a granular material for which the mechanical behaviour can be modelled by the discrete element method (DEM) in a high shear rate regime (Hansen and Brown, 1988). The complexity of the snow microstructure can be considered by feeding the DEM simulations with high-resolution 3D reconstructions of the snow sample obtained with μCT. The downside of this method is that it is time-consuming, and simulations can only be performed on small samples (up to a few centimetres). These simulations have nevertheless provided new insights on the snow mechanical behaviour, such as distinct resistance to confined compression for different microstructure properties (Hagenmuller et al., 2015) or identification of failures mode in a

https://doi.org/10.5194/tc-2023-30
Preprint. Discussion started: 2 March 2023
© Author(s) 2023. CC BY 4.0 License.


mixed mode loading (Mede et al., 2018b, 2020). Although these models appear capable of accounting for the role of the microstructure on the mechanical response, they still lack experimental confrontation.

This study aimed to evaluate a microstructure-based DEM model with experimental data of cone penetration tests. To address this goal, we modelled CPT on a realistic representation of the snow samples with DEM numerical simulations. The deformation induced by the CPT configuration (strain rate of about 10^2 s^{-1}, Reuter et al., 2019) belongs to the elastic-brittle regime (Narita, 1983; Floyer and Jamieson, 2010) and is therefore suitable for DEM simulation. The model has been designed to account for the snow properties and the snow microstructure acquired by µCT (Hagenmuller et al., 2015; Mede et al., 2018b, 2020). The results of the numerical model are confronted to results performed experimentally on snow samples (Peinke et al., 2020). We compared (1) the macroscopic force profile with relevant structural parameters and (2) the grain displacements induced by the cone penetration. A systematic sensitivity analysis to mechanical parameters of the contact law, including Young's modulus, the cohesion and the friction angle, was also performed with DEM to evaluate their influence on the mechanical behaviour and find the best combination of mechanical parameters to reproduce experimental results. Finally, the role of the microstructure is also investigated by performing the DEM simulations with different snow types. The evaluation of the numerical model provides the opportunity to better understand the mechanisms at work during the snow deformation in an elastic-brittle regime and better interpret CPT profiles.

We first present the experimental data set and the numerical model used to perform CPT. The data processing used to compare experimental and numerical results is also explained. The results of the DEM, the sensitivity analysis to mechanical parameters and the comparison to experimental results are then presented. The relevance of the DEM model and the limits of our approach are eventually discussed before concluding.

2 Methods

2.1 Experiments

The experimental data set used in this study has been acquired by Peinke et al. (2020) and is only briefly presented in this paper. The methodology comprises collection and preparation of snow samples, acquisition of high resolution micro-tomographic images and cone penetration tests (CPT).

2.1.1 Snow sample preparation

Blocks of natural snow were sampled in the French Alps near Grenoble and stored at -20°C in a cold room. The materials collected are representative of the variety of seasonal snow types (Table 1), namely rounded grains (RG), large rounded grains (RGlr), depth hoar (DH) and precipitation particles (PP), with distinct bulk densities and specific surface areas (SSA).

The samples were prepared in a cold room at -10°C by sieving the snow into aluminium cylinders, suitable for X-ray tomography (high thermal conductivity and relatively low X-ray absorption), of 2 cm height and 2 cm diameter. All samples were prepared at least 24 hours before the measurements in order for the bonds between grains to rebuild after sieving.

https://doi.org/10.5194/tc-2023-30
Preprint. Discussion started: 2 March 2023
© Author(s) 2023. CC BY 4.0 License.


2.1.2 Micro-Tomography (µCT)

Tomographic scans of each sample were acquired before and after performing the CPT to capture, respectively, the initial and final microstructure of the snow. An X-ray tomograph (DeskTom130, RX Solutions) operating at a pixel size of 15 µm pix^{-1}, a voltage of 80 kV and a current of 100 µA was used. During tomographic scanning, the samples were maintained at a constant and uniform temperature of -10°C in a cryogenic cell (CellDyM, Calonne et al. (2015)). Each scan, consisting of 1440 2D radiographs, was reconstructed to obtain 3D grayscale images representing the attenuation coefficients of the different materials composing the samples. The grayscale images were then transformed into binary (ice matrix – pore space) segmented images using an energy-based segmentation algorithm (Hagenmuller et al., 2013).

2.1.3 Cone Penetration Test (CPT)

Posterior to the initial micro-tomography scan, a CPT was performed on the snow samples using a modified SnowMicroPenetrometer (SMP version 4, Schneebeli and Johnson, 1998). The specific rod used by Peinke et al. (2020) displays a conic tip with an apex angle of 60° and a maximum cone radius equal to the rod radius R of 2.5 mm. The rod was inserted vertically into the snow sample at a constant penetration speed v of 20 mm s^{-1}. The resisting force applied on the rod was recorded every 4 µm of penetration increment (i.e. 5 kHz frequency). The SMP sensor (Kistler sensor type 9207) measures forces up to 40 N with a resolution of 0.01 N. The tip was stopped at depths between 7 and 15 mm, *i.e.* 5-13 mm above sample bottom, to avoid boundary effects (Peinke et al., 2020).

2.2 Numerical modelling

Snow is here considered as a granular cohesive material. Indeed, the high strain rate (> 10^{-4} s^{-1}) induced by the tip penetration in the snow sample leads to brittle deformations with inter-granular damage and grain rearrangements (Narita, 1983; Johnson and Hopkins 2005; Hagenmuller et al., 2015). We adopted an approach based on the discrete element method (DEM) to simulate the cone penetration tests in the measured snow samples. The mechanical model is based upon the work of Hagenmuller et al. (2015) and Mede et al., (2018a, b and 2019) and is performed with YADE solver (Šmilauer et al., 2015). This modelling approach is composed of three main steps: the generation of the initial conditions based on the measured snow microstructures, the definition of the contact law between the snow grains, and the setting of the boundary conditions to reproduce the CPT configuration.

2.2.1 Grain segmentation and grain shape representation

The DEM model was fed by the 3D ice-air images obtained with X-ray tomography. The continuous ice matrix was first segmented into individual grains based on geometrical criteria as described by Hagenmuller et al. (2013). The main idea of the approach is to detect potential mechanical weakness (i.e., the bonds) based on the principal minimal curvature κ_T and the contiguity parameter between the grains c_T. The threshold on curvature κ_T was set at 1.0 for RG, RGlr and DH samples and

https://doi.org/10.5194/tc-2023-30
Preprint. Discussion started: 2 March 2023
© Author(s) 2023. CC BY 4.0 License.

0.7 for PP sample (see Hagenmuller et al., 2013 for details). The contiguity parameter was set to 0.1 for all the samples (see Hagenmuller et al. (2013) for details).

The irregular shape of the grains was approximated by filling the grain volume with a population of overlapping spheres (Fig. 1). The position of these spheres were derived from the medial axis of the structure (Coeurjolly and Montanvert, 2017; Mede et al., 2018a) and redundant spheres were discarded based on a power diagram filter (Coeurjolly and Montanvert, 2017). The grain shape representation by a multitude of spheres preserves the capability of YADE to handle contact detection. However, a high number of spheres slows the numerical simulation down. We thus further decimated the number of spheres by approximating the grain volume. We only selected the spheres with a radius larger than R (voxel) and covering (in the sense of the power diagram) a large proportion of the grain volume (parameter S). A trade-off must be found between the error of the grain shape approximation, influencing the mechanical behaviour accuracy, and the number of spheres influencing the numerical cost of the simulations. A sensitivity analysis to this grain representation was conducted (Table S1, Fig. S1) to determine the optimal R and S parameters. The chosen R and S values for each snow type, associated with the volumetric E_V and mechanical E_M errors, can be found in Table 1. Eventually, the spheres belonging to the same grain were clumped together in rigid aggregate and constitute a single discrete element (DE).

Sample name	Snow type	Sieve size (mm)	Bulk density (kg m^{-3})	SSA (m^2 kg^{-1})	R (vx)	S	Number of spheres	Number of clumps	Number of initial cohesive interaction between clumps	E_v (%)	E_M (%)
RG	Rounded Grains	1.6	289	23.0	5	0.3	514917	27560	47736	42.3	18.0
RGlr	Large Rounded Grains	1	530	10.1	5	0.3	270143	8488	24005	14.6	9.2
DH	Depth Hoar	1.6	364	15.9	5	0.2	743546	11211	24258	24.7	12.7
PP	Precipitation Particle	1.6	91.3	53.5	2	0.5	1797567	95022	125805	32.2	9.6

Table 1: Overview of the snow samples analysed in this study and the respective grain shape representation chosen. The sample names were given according to the snow type classification (Fierz et al., 2009). The sample density and specific surface area (SSA) were derived from the micro-tomographic images (Peinke et al., 2020). The minimum radius of the sphere R and the minimum sphere coverage S were determined by sensitivity analysis presented in Sect. S1.1. The associated number of spheres, grains and cohesive grain-grain interaction are indicated. Finally the volumetric error E_V and the mechanical error E_M for each grain shape representation were calculated.

2.2.2 Interactions and contact law

The contacts between adjacent grains were identified during the grain segmentation phase. In the DEM simulations, the grain contacts were represented by several sphere-sphere interactions. The interactions between spheres were described by an elastic brittle cohesive contact law. The adhesion A, Eq. (1), the normal contact stiffness K_N, Eq. (2) and the shear contact stiffness K_S, Eq. (3) were initially set as:

https://doi.org/10.5194/tc-2023-30
Preprint. Discussion started: 2 March 2023
© Author(s) 2023. CC BY 4.0 License.


$$A = \mathrm{D} \times \mathrm{C}\,, \tag{1}$$

$$K_N = \frac{D \times E}{r_{mean}}, \tag{2}$$

$$K_S = \nu \times K_N\,, \tag{3}$$

with D the contact area between two spheres (m^2), weighting the bond magnitude between grains according to the spheres size, C the cohesion (Pa) of ice, E Young's modulus (Pa) of ice, r_{mean} (mm) the mean sphere radius of the numerical sample, which constitute a characteristic length of the grain shape representation of the sample and is used to scale the normal stiffness in order that all the sphere-sphere interactions between two grains fails at the same moment, and finally, ν the Poisson's ratio of the material.

The forces acting on the spheres in contact depend on the stiffness of the material (Mede et al., 2020). The tensile force F_N, Eq. (4), is proportional to the distance between two considered spheres x_N:

$$F_N = K_N x_N \ \leq A\,, \tag{4}$$

The contact between spheres exists as long as F_N remains below the adhesion value A. Once the cohesion is broken in tension, the bond is not cohesive anymore also in the shear direction. The shear force F_S, Eq. (5), display a linear dependency to the relative displacement of the sphere to the considered neighbouring sphere x_S with a maximal shear force limited by the sum of adhesion and Mohr-Coulomb friction:

$$F_S = K_S x_S \ \leq A + \ F_N \times \tan\varphi\ \ , \tag{5}$$

where φ is the friction angle. As long as the spheres remain in contact after the cohesion has been broken, Mohr-Coulomb friction remains active in shear.

The contact force, stiffness and adhesion of grains in contact correspond to the sum of the respective values of all the spheres in contact. At the initial step of the simulation, all contacts are cohesive. While the numerical sample deforms, new clumps positions are computed with the momentum conservation equation. Grain motion can potentially lead to cohesive interactions failure and creation of new interactions. New interactions created during the computation are frictional only (no cohesion).

2.2.3 Boundary conditions

In order to evaluate the DEM model we have implemented a CPT configuration similar to the experimental set-up used by Peinke et al. (2020) (Fig. 1). The snow sample is contained in a rectangular box opened at the top. The box displays the following dimensions, about 12.4 mm along the x and y axis and about 15 mm along the z axis. The box size along the horizontal plane W has been reduced compared to the 20 mm diameter of the sample holder used by Peinke et al. (2020). This choice has been motivated first to simplify the geometry with a rectangular numerical sample and second to reduce the number of spheres decreasing the computational time. A sample size sensitivity analysis has been performed to ensure border effects are not introduced by reducing the sample size (Fig. S2). The tip displays a maximal radius r of 2.5 mm and an apex angle of

https://doi.org/10.5194/tc-2023-30
Preprint. Discussion started: 2 March 2023
© Author(s) 2023. CC BY 4.0 License.

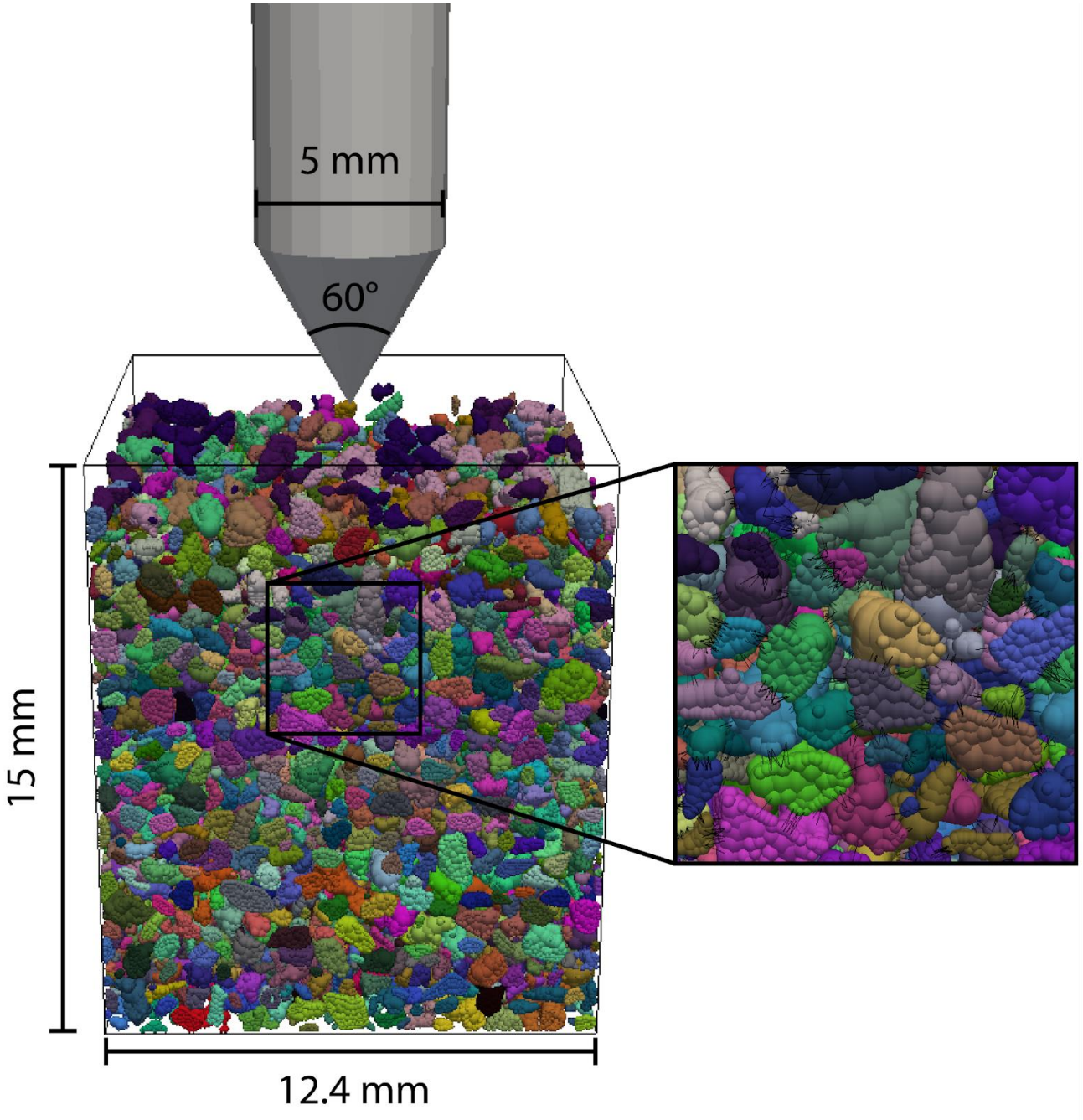

215 60°. The tip, initially in a centred position at the box surface, is travelling downward, through the sample, at a constant speed of 20 mm s^{-1}. The simulation stops when the tip reaches the bottom of the box. The walls (box and tip) are represented by facets with rigid boundary conditions. The gravity is set to 9.81 m s^{-2}.

https://doi.org/10.5194/tc-2023-30
Preprint. Discussion started: 2 March 2023
© Author(s) 2023. CC BY 4.0 License.

Figure 1: Visualisation of CPT modelling with DEM model for the RGlr sample. The tip is travelling downward at a constant speed of 20 mm s^{-1}. Grains are composed of overlapping spheres clumped together (single colour). The zoomed window focuses on DEM grains. Black lines correspond to cohesive interactions between spheres of adjacent grains.

The stability of the explicit integration scheme of the continuum equations is ensured by estimating the critical time step, Eq. (6) based on the propagation speed of elastic waves in the sample (Zhao, 2017):

$$\Delta t_{cr} = min\left(\frac{m_i}{K_i}\right)^{0.5} , \quad (6)$$

with m_i and K_i the mass and stiffness of the discrete element i. The grain mass m_i can be artificially increased to increase the time step (Hagenmuller et al., 2015). A numerical sensitivity analysis (Fig. S3) has shown that increasing the mass by a factor f of 100 does not affect the simulation results. Finally, Cundall's non viscous damping coefficient of 0.05 was applied according to the results of a numerical sensitivity analysis (Fig. S4).

2.2.4 Input parameters

The density of the ice grains was set to $\rho = f \times 917$ kg m^{-3}. The contact law parameters were derived from typical values measured on ice. The Poisson coefficient ν was set to 0.3 (Schulson and Duval, 2009). The typical Young's modulus E, cohesion strength C and friction angle tan(φ) values for the ice are usually evaluated respectively around 1 x 10^{10} Pa, 1 x 10^6 Pa and 0.2 (Gammon et al., 1983; Schulson and Duval, 2009). For this study, we performed a sensitivity analysis of the simulation to these parameters to get insights into the model behaviour. The mechanical parameters were either directly derived from the values obtained on ice or adjusted to fit the experimental measurements. We performed the analysis over ranges of 1 x 10^8-1 x 10^{10} Pa for E, 5 x 10^5-5 x 10^6 Pa for C and 0.2-0.5 for tan(φ), respectively. Note that the range of Young modulus E ensures small grain overlap, which satisfies the rigid grain assumption (Fig. S5).

Boundary conditions		
Sample width	W	13 mm
Tip radius	R	2.5 mm
Cone apex	a	60°
Tip velocity	v	20 mm s^{-1}
Gravity	g	9.81 m s^{-2}
Numerical parameters		
Time step	dt	~ 1 x 10^{-6}-1 x 10^{-8} s
Mass factor	f	100
Non-viscous damping coefficient	$\boldsymbol{\lambda}$	0.05
Material properties		
Grain density	$\boldsymbol{\rho}$	917 x 10^2 kg m^{-3}
Poisson coefficient	$\boldsymbol{\nu}$	0.3
Friction angle	tan(φ)	0.2–0.5 (default value 0.2)
Young's modulus	E	1 x 10^8–1 x 10^{10} (default value 1 x 10^9) Pa
Cohesion	C	5 x 10^5–5 x 10^6 (default value 1 x 10^6) Pa

Table 2: Input parameters used for the simulation presented in this paper.

https://doi.org/10.5194/tc-2023-30
Preprint. Discussion started: 2 March 2023
© Author(s) 2023. CC BY 4.0 License.


2.3 Data processing

The main outputs of the DEM simulations are the resisting force exerted by the grains on the penetrometer and the displacement of the grains induced by the cone penetration. These results can be directly compared to the experimental measurements to evaluate the DEM model.

2.3.1 Force sampling

The sum of the forces along the z-axis applied on all the facets constituting the tip (cone and rod) is recorded at each time step. To match the sampling frequency of the SMP (i.e., 4 µm), the numerical values are averaged over windows of 4 µm. This smoothing is useful to avoid high-frequency fluctuations linked to the very small time step used in DEM. To ensure a relevant comparison, numerical and experimental force profiles are then re-sampled by linear interpolation over a regular grid with a step of 4 µm over the same depth. The profiles span from a depth of 0 mm to the chosen maximum depth, which, in our study, is set to 7 mm (i.e., 1750 points).

2.3.2 Statistical indicators

Quantitatively, the DEM numerical model is evaluated by a comparison with experimental force profiles in terms of three statistical indicators: the mean force F, the standard deviation σ of the force fluctuations, and the correlation length l. The standard deviation σ is calculated on a detrended force profile obtained by subtracting the mean force value calculated over a rolling window Δz = 3 mm, to take only into account the force fluctuations and not the global trend of the profile. The correlation length l (mm) is also computed on the detrended force profiles. In our study, the snow samples exhibit a rather homogeneous structure allowing us to consider l constant over depth (Peinke et al., 2019). These three statistical indicators have been chosen because they are easily quantifiable and commonly used to describe force profiles obtained by CPT in snow (Johnsson and Schneebeli, 1999; Löwe and van Herwijnen, 2012; Peinke et al. 2019). They constitute key parameters to derive additional microstructural properties based on Poisson shot noise models (Löwe and van Herwijnen, 2012; Peinke et al. 2019). To select the set of mechanical parameters (E, C and tan(φ)) providing the best fit to the experimental measurements among the tested values (Table 2), the total error is computed as the root square of the addition of the squared relative errors of the structural parameters obtained with numerical modelling compared to the ones obtained for experimental measurements. We attribute a weight of 2 to the mean macroscopic force relative error as we assume it is the main parameter to reproduce. The set of mechanical parameters for which the lowest value of total error is obtained, is considered as the most representative of the physical characteristics of the different types of snow samples.

https://doi.org/10.5194/tc-2023-30
Preprint. Discussion started: 2 March 2023
© Author(s) 2023. CC BY 4.0 License.


2.3.3 Grain displacement analysis

The grain position is recorded every ~0.4 mm in the DEM simulations. The total displacement and the displacement path can therefore be reconstructed for each grain. Due to the thermodynamically active nature of the snow, the incremental record of the snow sample state during the experimental CPT was not possible. Therefore we only measured the initial (before CPT) and the final state (after CPT) of the snow sample. Grain tracking, applied to the micro-tomographic images, has been performed by Peinke et al. (2020) providing the total displacement of the identified grains. We compared the total displacement between the CPT experiments and the DEM simulations at the same penetration depth, i.e. maximal penetration measured experimentally.

The profiles of vertical and radial displacements were averaged around the cone axis and on the height of an area located between the top section of the cone and the sample surface. A displacement threshold of 0.03 mm is set to define the deformation zone (DZ) (Peinke et al., 2020). Only the radial profiles were compared to the experimental results as we suspect the vertical profiles derived from µCT scans might be misleading (Peinke et al. 2020). Indeed, before acquiring the post-CPT µCT scans, the tip was removed from the snow. This procedure is performed about one hour after the tip penetration in order for the bonds between ice grains to form by sintering to limit the grains displacement while the tip is removed. Despite this precaution some grains in contact with the tip might be dragged upward due to the tip-grain friction. Therefore, the grain trajectory observed on the pre- and post CPT µCT scans could enhance the upward component of the vertical displacement for the experimental results, especially for the larger grains.

3 Results

3.1 Cone Penetration Tests on numerical samples with DEM

This section shows an example of results obtained for a DEM simulation of the CPT on the numerical snow sample RG with the following mechanical parameters: $E = 1 \times 10^9$ Pa, $C = 5 \times 10^6$ Pa and $\tan(\varphi) = 0.2$ (Table 3). The results for the other snow samples are shown in Sect. S2.1.

https://doi.org/10.5194/tc-2023-30
Preprint. Discussion started: 2 March 2023
© Author(s) 2023. CC BY 4.0 License.

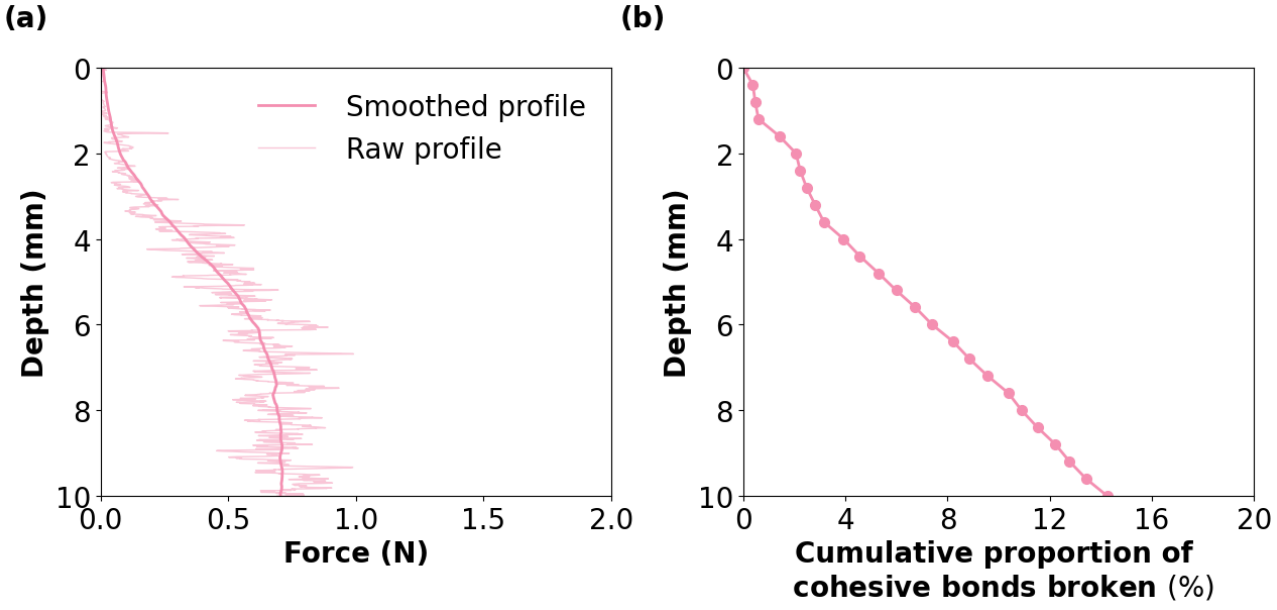

Figure 2: (a) Force as function of penetration depth (light line) obtained for the RG sample. The superposed smoothed profile (bold line) corresponds to the averaged force value over a rolling window of 3 mm. (b) Cumulative percentage of cohesive bonds broken as function of tip penetration depth. The initial number of cohesive bonds is indicated in Table 1. Results are obtained with the mechanical parameters given in Table 3.

The simulated penetration force globally increases with depth, with high-frequency fluctuations (Fig. 2 (a)). The force profile displays a 'S' shape with three stages: 1) up to ~ 3.5 mm depth the profile is convex, 2) between ~ 3.5 and ~ 6 mm depth, the increase of force with depth is almost linear, and 3) for larger depths, the force reaches a nearly constant value. A similar behaviour is observable for all the samples (Figs. S6 (a), S8 (a), S10 (a)), with slight changes in the transition depths between the different stages.

The penetration of the tip induces bond failures in the simulated samples. The number of bond failures globally increases at a constant rate with penetration depth (Fig. 2 (b)). Overall, for the RG sample, about 15% of the cohesive interactions broke over 10 mm of penetration, corresponding to an average rate of ~710 bond failures mm^{-1}. This bond failure rate is variable among the samples, reaching 1200 bond failure mm^{-1} for RGlr sample (Figs. S6 (b), S8 (b), S10 (b)). In detail, for the RG sample, we notice an increase of bond failure intensity at around 3.5 mm penetration depth (Fig. 2 (b)) coinciding with the transition between the first and second stages observed in the force signal (Fig. 2 (a)). Bond failure intensity then remains unchanged as the macroscopic force reaches its steady-state value. Similar characteristics are observed for the other snow types (Figs. S6, S8, S10).

https://doi.org/10.5194/tc-2023-30
Preprint. Discussion started: 2 March 2023
© Author(s) 2023. CC BY 4.0 License.

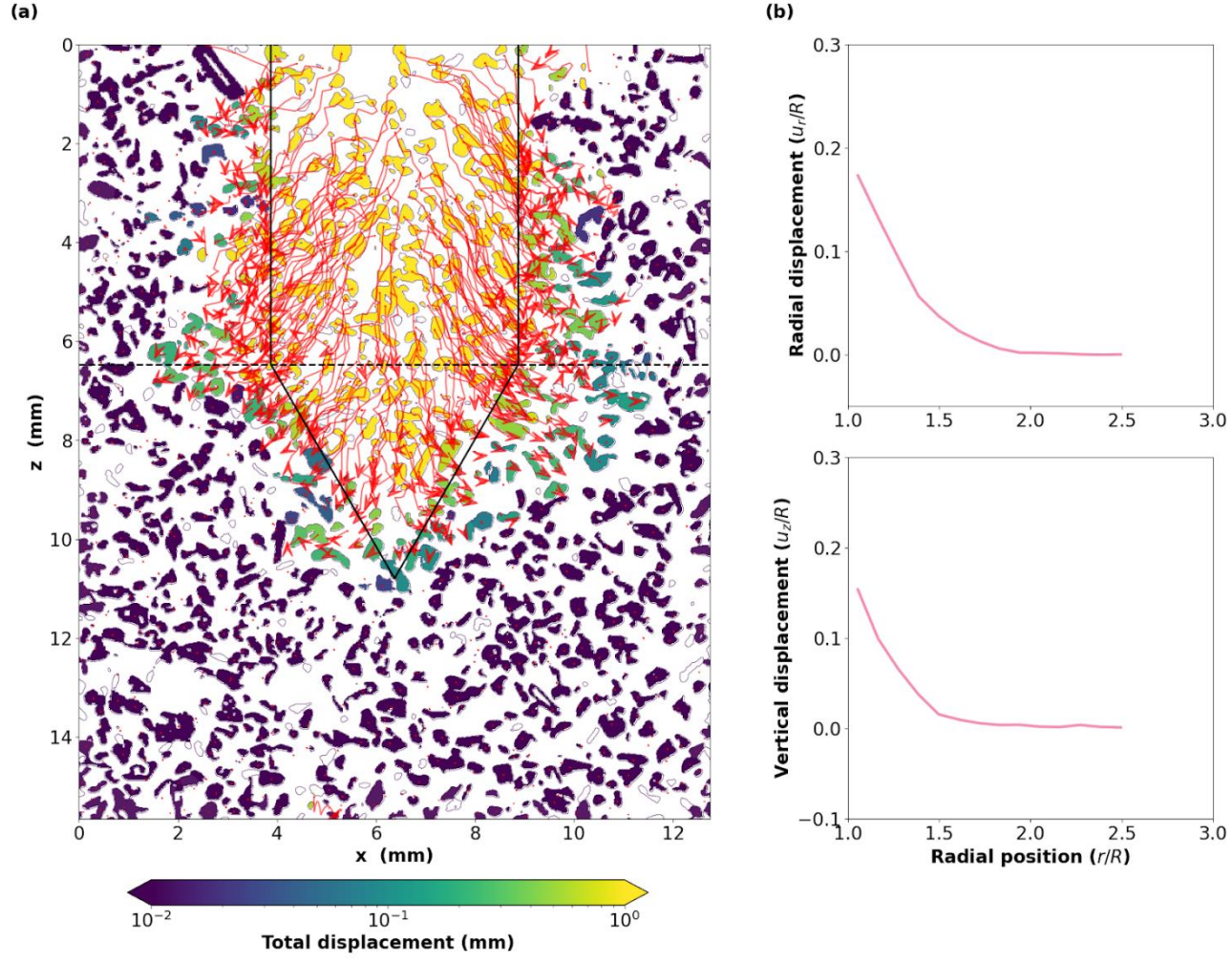

Figure 3: (a) Simulated grain displacement map of the RG sample. The red arrows indicate the grain trajectories while the tip is penetrating (sampling = 0.4 mm). White grains correspond to grains not represented in the DEM simulation. The final tip position is indicated by the black solid lines. The horizontal black dashed line indicates the cone top. (b) Radial (upper panel) and vertical (lower panel) displacement profiles for the RG sample. These profiles represent averages computed from sample surface to the cone top. By convention, downward (respectively upward) movement corresponds to positive (respectively negative) values of vertical displacement. Results are obtained with the mechanical parameters given in Table 3.

DEM simulations also allow tracking grain positions while the tip is penetrating into the numerical sample. Figure 3a shows the total displacement of the grains and their respective trajectories for the RG sample. The largest displacements (up to several mm) are observed for grains initially located on the trajectory of the tip. Around the tip the displacements are < 1 mm and are mainly localised close to the tip. Grain trajectories indicate that grains are pushed downward from each side of the tip. Grains initially located on the penetrometer axis display a quasi-straight vertical trajectory. The trajectories become more radial and curved away from the tip medial axis, with the grains being also pushed aside. Around the cone, grain trajectories are

https://doi.org/10.5194/tc-2023-30
Preprint. Discussion started: 2 March 2023
© Author(s) 2023. CC BY 4.0 License.

predominantly straight, with an almost radial orientation at the cone top and a more vertical orientation near the tip. Both radial and vertical displacement profiles show a pronounced decreasing trend, and reach zero at a radial position of about 1.7R (Fig. 3 (b)). The vertical profile attests of a dominant downward movement of the grains close to the tip. Similar observations are made for the DH sample (Fig. S9). In contrast, for the RGlr sample, vertical displacements are smaller and oriented slightly upwards on average for the mechanical parameters chosen here (Fig. S7).

3.2 Sensitivity to mechanical parameters

The influence of the mechanical parameters (Young's modulus, cohesion, friction angle) describing the contact law, on the simulations has been systematically explored. The force profiles obtained for the different values of the parameters within the explored ranges (Table 2) are presented for the RG sample in Figure 4, and a synthetic plot of the sensitivity of the statistical indicators to these parameters is presented in Figure 5. The results for other samples as well as Table S2 summarising all the statistical indicators obtained, can be found in Sect. S2.3.

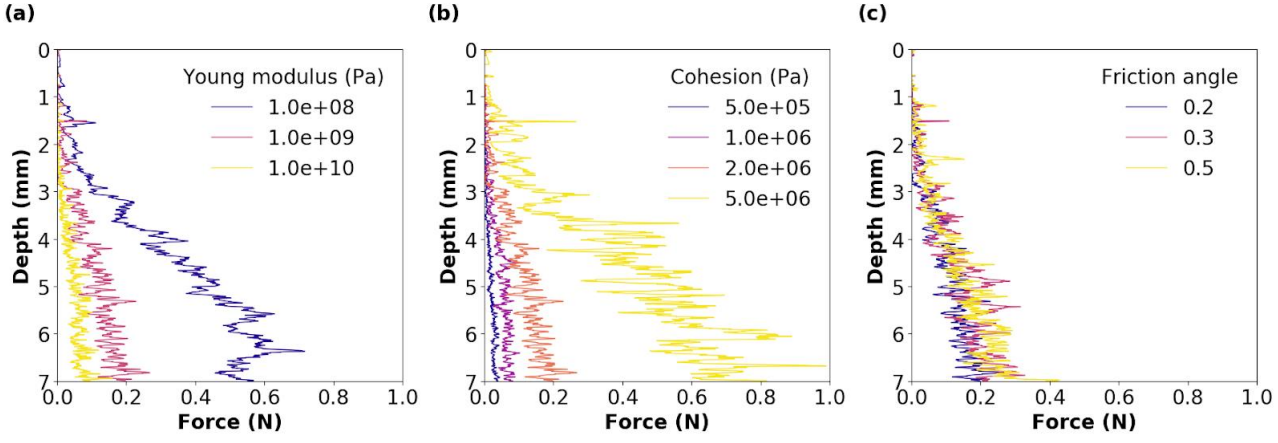

Figure 4 : Influence of mechanical parameters on the simulated force profile. The sensitivity analysis has been performed on (a) Young's modulus E (Pa) (for C = 2.0 x 10^6 Pa and tan(φ) = 0.2), (b) the cohesion C (Pa) (for E = 1.0 x 10^9 Pa and tan(φ) = 0.2) and (c) the friction angle tan(φ) (for E = 1.0 x 10^9 Pa and C = 2.0 x 10^6 Pa). Results presented here correspond to the RG sample.

First, we observe that increasing Young's modulus decreases the macroscopic force (Fig. 5 (a)). The influence of Young's modulus on the standard deviation is more complex and displays a co-dependency with the cohesion values (Fig. 4 (b)). From low to high cohesion values, the standard deviation evolves from a decreasing to an increasing trend with Young's modulus, respectively. The influence of Young's modulus on the correlation length is weak (Fig. 4 (c)), as we observe mainly quasi-constant values over Young's modulus values. However, we notice a decreasing trend for large Young's modulus and low cohesion. Regarding the influence of the cohesion and friction angle, increasing these parameters increases the three statistical indicators.

https://doi.org/10.5194/tc-2023-30
Preprint. Discussion started: 2 March 2023
© Author(s) 2023. CC BY 4.0 License.

The Cryosphere Discussions
Open Access
EGU

Aside from changes in absolute values, the evolution of force profiles (Figs. S14, S18 and S22) and statistical indicators (Figs. S15, S19 and S23) follow similar trends for all the samples, attesting to a moderate influence of the snow type. Nevertheless, it has to be noticed that the influence of Young's modulus on the correlation length is more pronounced for the RGlr (Figs. S14, S15) and the DH (Figs. S18, S19) samples. We must highlight that due to large computing times, fewer parameter values have been explored for large Young's modulus. It is the case especially for the PP sample for which no numerical simulations for a Young's modulus of 1 x 10^{10} Pa has been performed as computing times were too long (E = 1 x 10^{8} Pa, t ~ 4 months and E = 1 x 10^{9} Pa, t ~ 10 months) to be achieved.

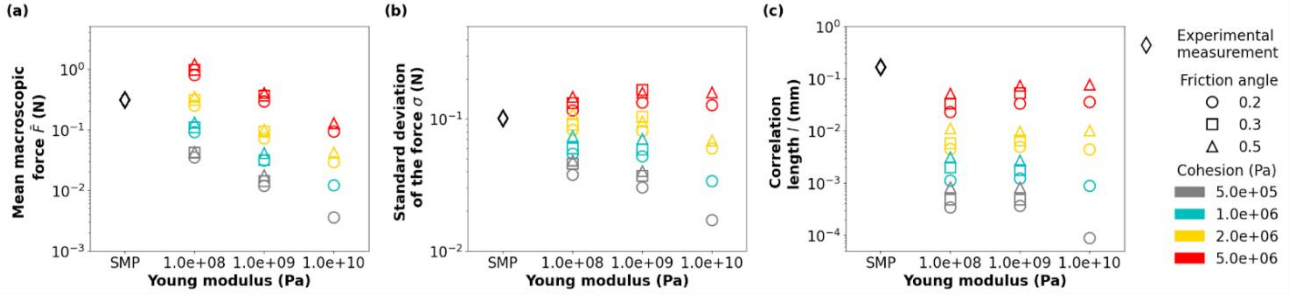

Figure 5: Evolution of statistical indicators as function of Young's modulus, cohesion and friction angle: (a) Mean macroscopic force, (b) standard deviation of the force, and (c) correlation length. The experimental results (black diamonds) have been added to the plots. Results presented here correspond to the RG sample.

The number of broken bonds with tip penetration depth appears insensitive to Young's modulus (Figs. S12 (a), S16 (a), S20 (a), S24 (a)) and is slightly reduced when cohesion increases (Figs. S12 (b), S16 (b), S20 (b), S24 (b)). Conversely, the friction angle shows a pronounced influence, with an increase in bond failures when this parameter increases (Figs. S12 (c), S16 (c), S20 (c), S24 (c)).

Finally, the influence of all the mechanical parameters on the radial grain displacement profiles is negligible (Figs. S13, S17, S21, S25). Young's modulus has no influence on the vertical grain displacement. Cohesion only plays a role on the vertical displacement profile for the RGlr sample by enhancing upward movements. Larger friction angles tend to increase the downward movement of the grains close to the tip for all the snow types.

3.3 Comparison of DEM results with experimental measurements

The results of the DEM numerical model are compared to the experimental results to evaluate its predictive capability. First, it can be noted that, for the values of the mechanical parameters tested, the orders of magnitude of the statistical indicators obtained numerically and experimentally are similar for most of the cases (Figs. 5, S15, S19, S23, Table S2), proving the DEM model can reproduce the main CPT force profile characteristics. However, we highlight the difficulty to match the three statistical indicators at once for a given combination of the three mechanical parameters. Hence, for the RG sample (Fig. 5), the DEM simulations fit well with the mean macroscopic force and the standard deviation of the measured

https://doi.org/10.5194/tc-2023-30
Preprint. Discussion started: 2 March 2023
© Author(s) 2023. CC BY 4.0 License.


force profiles, but tend to underestimate the correlation length. For the RGlr and DH samples (Figs. S15, S18), all the statistical indicators can be reproduced individually, but not for one single combination of the mechanical parameters tested. For the PP sample, the experimental mean force can be well reproduced numerically, but the correlation length is underestimated (Fig. S23). The standard deviation can be approached for large Young's modulus and cohesion values. However the dataset is incomplete to provide a strong insight.

Sample	E (Pa)	C (Pa)	tan(φ)	Error F	Error σ	Error l	Total error
RG	1×10^{9}	5×10^{6}	0.2	-5.0×10^{-2}	3.2×10^{-1}	-8.0×10^{-1}	8.6×10^{-1}
RGlr	1×10^{10}	2×10^{6}	0.2	-2.9×10^{-1}	-5.5×10^{-1}	-1.2×10^{-1}	7.0×10^{-1}
DH	1×10^{9}	2×10^{6}	0.3	2.0×10^{-1}	-3.3×10^{-1}	-6.7×10^{-1}	8.0×10^{-1}
PP	1×10^{8}	2×10^{6}	0.2	4.5×10^{-2}	-3.9×10^{-1}	-9.9×10^{-1}	1.1×10^{0}

Table 3: Selected combination of mechanical parameters for RG, RGlr, DH and PP samples. The values of Young's modulus E, cohesion C and friction angle tan(φ) correspond to the combination that yields the lowest total error on the statistical indicators (mean force F, standard deviation, correlation length l) measured experimentally. Error values for all the mechanical parameters combinations tested are indicated in Table S2.

Based on the sensitivity analysis (Sect. 3.2.3.), we selected the combination of the three mechanical parameters that minimises the total error for the different samples (Tables 3, S2). The associated force profiles produced by the DEM simulations (referred to as 'Numerical simulation 1') are compared with the experimental profiles in Fig. 6. From a qualitative point of view, a good match is obtained between these numerical and experimental force profiles. For the RG sample, the macroscopic force is well reproduced but the standard deviation is slightly overestimated and the correlation length is slightly underestimated (Figs. 5, 6 (a), Table 3). Note that the mean force obtained numerically is underestimated in the first 3.5 mm of penetration compared to the experimental data. The experimental profile appears quasi-linear in this upper section, and does not display the S-shape observed on the numerical profile (Sect. 3.1.) for the range of depth presented here. However, observing the force profile over a larger depth range allows us to observe this 'S' shape (Fig. S26). Both the experimental and numerical force profiles then reach a quasi-steady state value at about the same depth (~ 6 mm). For the RGlr sample, the correlation length is well reproduced, while the mean force is slightly underestimated and the standard deviation is underestimated by a factor of ~ 0.5 (Figs. S15 and 6 (b), Table 3). It appeared difficult to reproduce the amplitude of force fluctuations visible in the upper section (from 0 to 4 mm) of the experimental profile. Both experimental and numerical profiles present a 'S' shape with a first slope change at around 3 mm of penetration. The simulations do not reproduce the force decrease after 6 mm observed in the experiments. For the DH sample, the mean macroscopic force is well reproduced. The standard deviation is slightly underestimated and the correlation length is underestimated by more than 60% (Figs. S19, 6 (c), Table 3). The numerical results miss the large force peaks observed in the upper part of the profile. Yet, it appears that the simulations fairly reproduce the general shape of the experimental profile. Finally, for the PP sample, the mean macroscopic force is well reproduced, while the standard deviation (60%) and correlation length (1 order of magnitude) are underestimated (Figs. S23 and 6 (d), Table 3).

https://doi.org/10.5194/tc-2023-30
Preprint. Discussion started: 2 March 2023
© Author(s) 2023. CC BY 4.0 License.

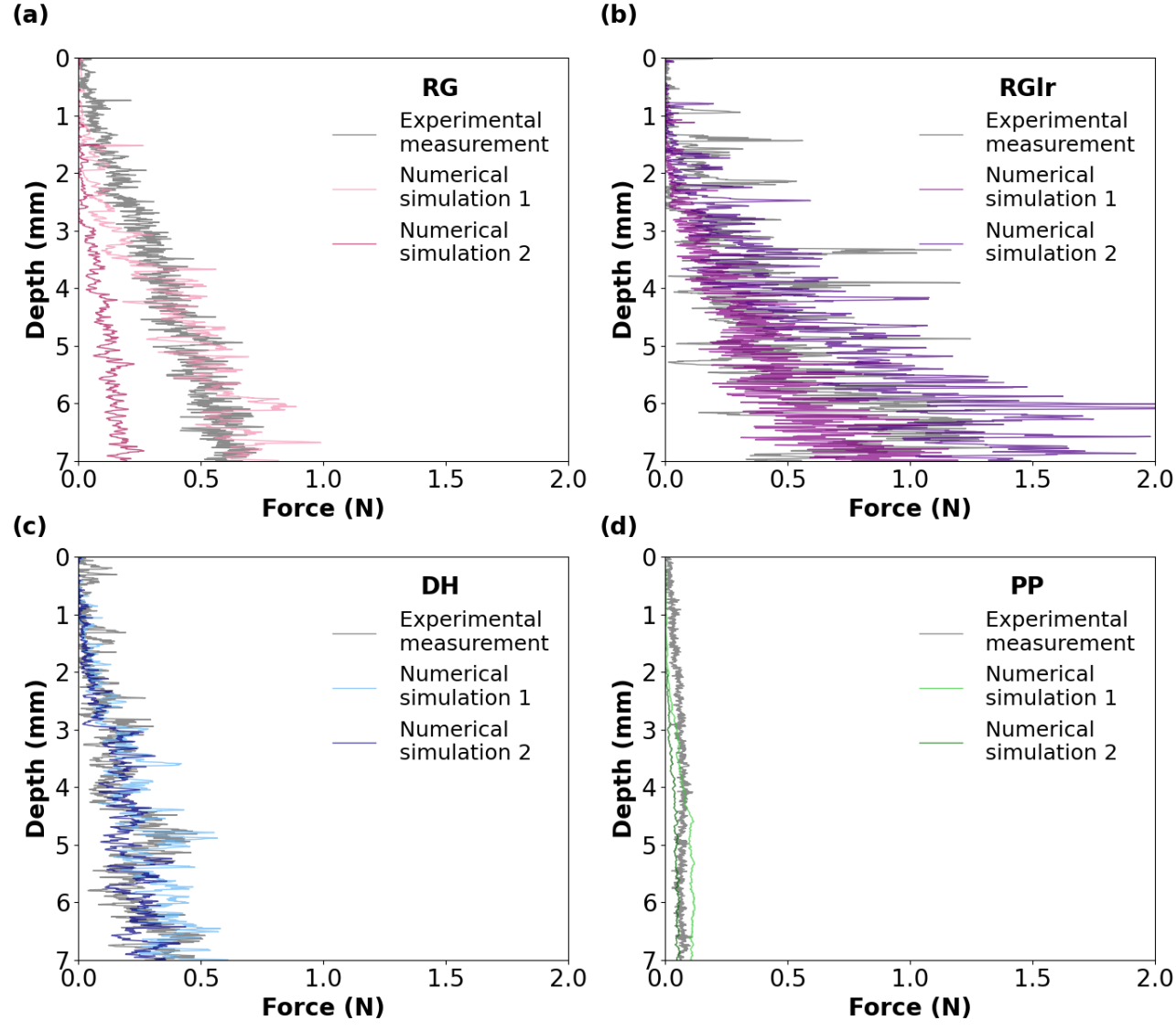

Figure 6: Experimental (grey) and numerical (coloured) CPT force profiles obtained for (a) RG, (b) RGlr, (c) DH, and (d) and PP samples. The "Numerical simulation 1" profiles correspond to the best fit of mechanical parameters for each sample (Table 3), while "Numerical simulation 2" profiles correspond to the overall best fit of mechanical parameters for samples RG, RGlr, DH and PP ($E = 1 \times 10^9$ Pa, $C = 2 \times 10^6$ Pa and $\tan(\varphi) = 0.2$, Table S2).

In addition, we also selected the single set of mechanical parameters that minimises the total error on RG, RGlr, DH and PP samples. Corresponding values are: $E = 1 \times 10^9$ Pa, $C = 2 \times 10^6$ Pa and $\tan(\varphi) = 0.2$. The respective errors for each sample can be found in Table S2. In general, the associated force profiles computed numerically agree fairly well with the experimental results ('Numerical simulation 2' in Fig. 6). For the RG sample, the standard deviation is well reproduced, while the mean macroscopic force and correlation length are significantly underestimated (Figs. 4, 5 (a), Table S2). For RGlr, the agreement

https://doi.org/10.5194/tc-2023-30
Preprint. Discussion started: 2 March 2023
© Author(s) 2023. CC BY 4.0 License.

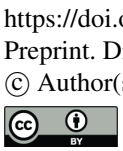

is acceptable for the three statistical indicators (relative errors between 39% and 47%). For DH, the mean macroscopic force is well reproduced, while the standard deviation is slightly underestimated (factor of 0.4) and the correlation length is underestimated (by about 80%). Finally, for the PP sample, the mean macroscopic force and the standard deviation are underestimated by about 50% and the correlation length is underestimated by about 100% (Figs. S23 and 6 (d), Table 3).

425

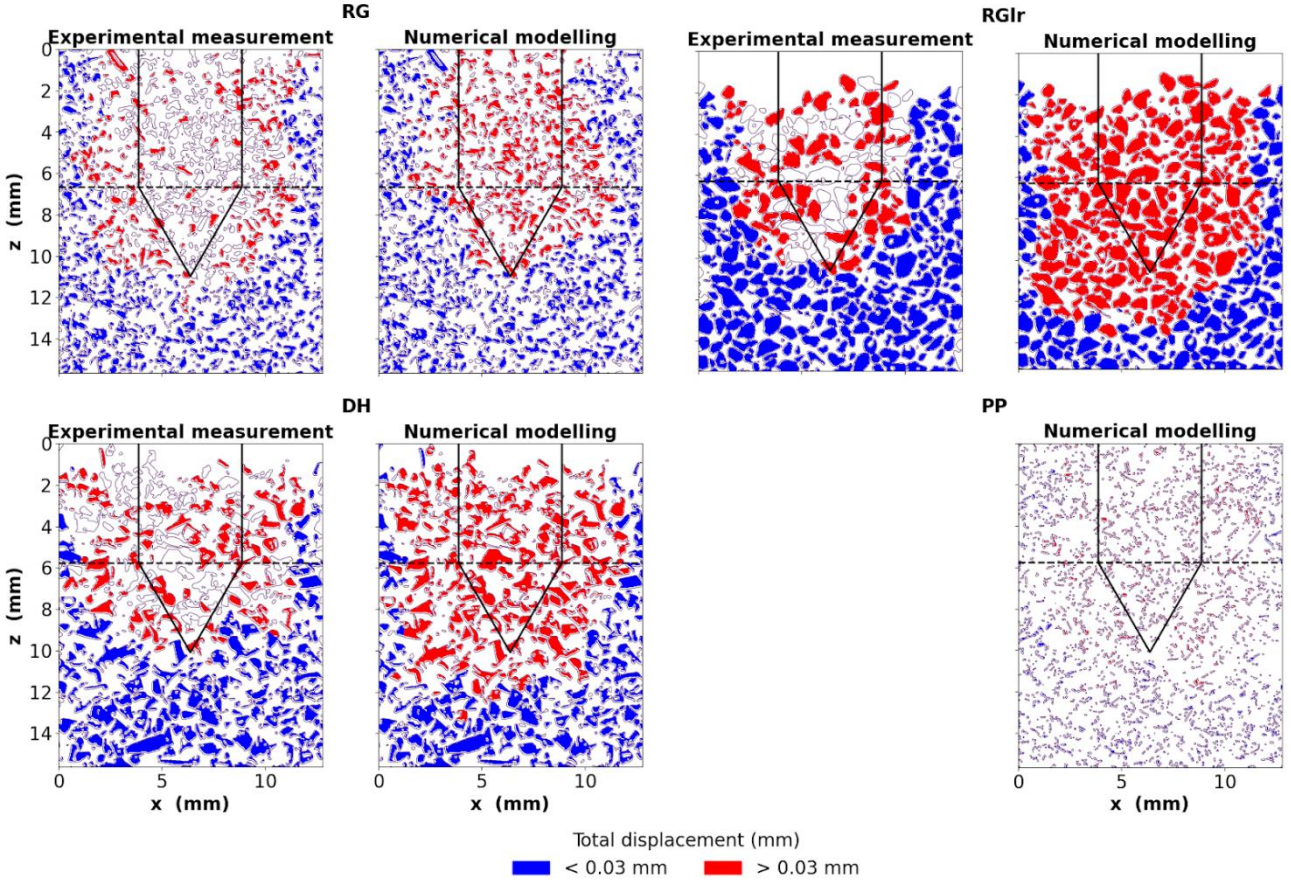

Figure 7: Total displacement maps obtained experimentally with µCT (left panel) and numerically with DEM simulation (right panel) for RG, RGlr, DH and PP samples. A displacement threshold at 0.03 mm has been set to define the deformation zone (Peinke et al., 2020). White grains correspond to non-trackable grains in µCT scans (Peinke et al., 2020) and deleted grains in the DEM
430 **simulations. The tip position is indicated with black solid lines. The horizontal black dashed line indicates the cone top. Displacement profiles shown in Fig. 8 are computed from the sample surface to the cone top. Numerical results are obtained with the combination of mechanical parameters indicated in Table 3. No experimental map is presented for the PP sample due to the difficulties to apply the grain tracking algorithm for this sample.**

435 Qualitatively, the numerical and experimental displacement fields present similar patterns for all snow types and both sets of selected mechanical parameters (Figs. 7 and S27). For the RG sample, the overall shape of the deformation zone is well reproduced by the simulations. The largest discrepancies are observed for the RGlr sample, for which the radial and vertical

https://doi.org/10.5194/tc-2023-30
Preprint. Discussion started: 2 March 2023
© Author(s) 2023. CC BY 4.0 License.

extension and distribution of the deformation zone differ from the data derived from µCT scans. The radial displacement obtained numerically displays a more linear trend compared to the arcuate shape of the experimental radial displacement profile (Fig. 8). For the DH sample, the radial extension of the deformation zone is well reproduced by the simulations, but the vertical extension tends to be overestimated. Finally, the numerical results obtained for the PP sample could not be compared to experimental measurements as the grain tracking algorithm is not applicable on these small grains (Peinke et al., 2020). The numerical results attest of the accordance of the deformation zone with other numerical profiles obtained for other snow types.

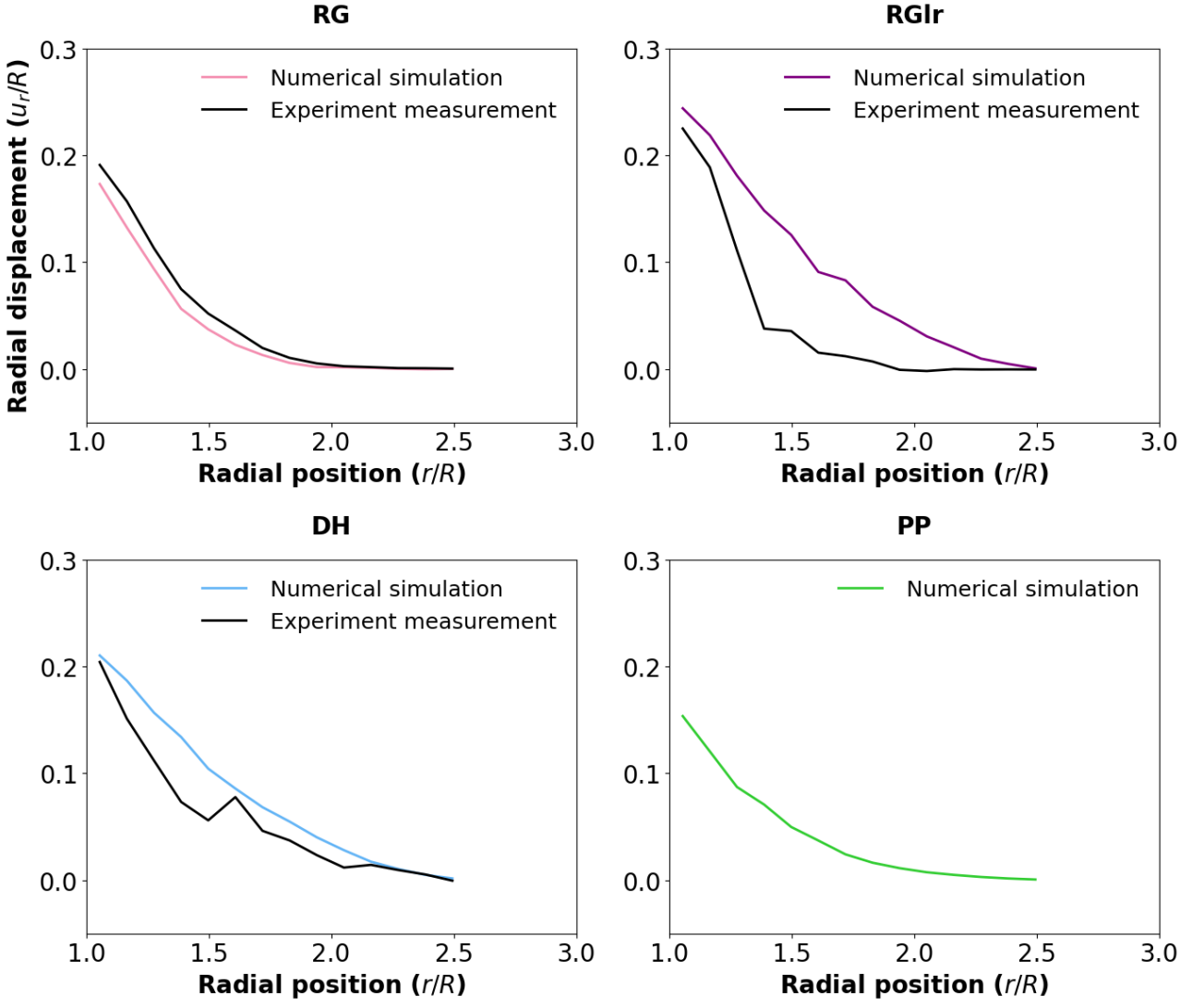

Figure 8: Radial displacement profiles obtained experimentally (black) and numerically (coloured) for RG, RGlr, DH and PP. Numerical results are obtained with the combination of mechanical parameters indicated in Table 3.

https://doi.org/10.5194/tc-2023-30
Preprint. Discussion started: 2 March 2023
© Author(s) 2023. CC BY 4.0 License.


Radial displacement profiles obtained with the DEM numerical model are overall in good agreement with their experimental counterparts (Fig. 8). Consistently with the displacement maps, the largest discrepancy is observed for the RGlr sample. In contrast, RG and DH samples show a very good agreement with experiments. The DZ (displacement threshold set at 0.03 mm) obtained from numerical simulations extend radially up to 1.7R, 2.2R, 2.2R and 1.8R for RG, RGlr, DH and PP samples respectively. The DZ obtained from CT scans extend up radially up to 1.8R, 1.7R and 2.2R for the same samples.

4 Discussion

4.1 Evaluation of the DEM model

We used three mechanical parameters, namely Young's modulus, the cohesion and the friction angle, to adjust the simulated force profiles to the experimental results. The numerical model could satisfactorily reproduce the mechanical response of all studied numerical samples with a single set of mechanical parameters ($E = 1 \times 10^9$ Pa, $C = 2 \times 10^6$ Pa and $\tan(\varphi) = 0.2$) (Fig. 6), indicating that the characteristics of the force profiles are mainly dependent of the snow microstructure.

It should also be noted that the values of the mechanical parameters obtained by adjusting the model on the experimental data (either globally for all samples, or for each sample individually, Table 3) are reasonably close to the mechanical properties of ice. Young's modulus of ice is measured between 9×10^9 Pa and 10×10^9 Pa (Gammon et al., 1983), while our selected values range between 1×10^9 Pa and 1×10^{10} Pa (except for PP sample). In practice, the numerical Young's modulus used in YADE software to parameterize the contact stiffness does not directly correspond to the physical Young's modulus of the material. In particular, the numerical Young's modulus may depend on the grain shape representation and/or the choice of the contact law. Nevertheless, the fact that the numerical value of E is close to that of ice provides good confidence that the DEM model and the used contact law (Eq. (1), Eq. (2), Eq. (3)) correctly capture the physical processes at play. Similarly, the numerical cohesion values ranging between 2×10^6 Pa and 5×10^6 Pa are in agreement with typical cohesion values measured on ice (in the range 2×10^6 Pa to 6×10^6 Pa, Schulson and Duval, 2009). Finally, numerical friction angles appear to be on the order of 0.2 – 0.3, while values measured experimentally are generally ranging from 0.02 to 1 (Fish and Zaretsky, 1997; Maneno and Arakawa, 2004). All these results reinforce the DEM model credibility.

We acknowledge that the mechanical parameters obtained from minimising the errors on the statistical indicators do not necessarily represent optimal values, in the sense that only a limited number of parameter sets could be tested. In particular, due to a high computational cost, few simulations performed with $E = 1 \times 10^{10}$ Pa were achieved for RG, RGlr and DH samples. Based on the sensitivity analysis, a proper inversion procedure could be developed to retrieve true optimal values of the mechanical parameters. This would provide more robust elements to determine whether a single set of mechanical parameters can be used to fit the experimental results of all snow types, or whether these mechanical parameters differ according to the snow types. In our current analysis, the answer to this question remains ambiguous. Note that ice is a polycrystalline material whose mechanical behaviour can be strongly anisotropic depending on the ice structure (Fish and

https://doi.org/10.5194/tc-2023-30
Preprint. Discussion started: 2 March 2023
© Author(s) 2023. CC BY 4.0 License.


Zaretsky 1997; Thorsteisson, 2001; e.g. Maeno and Arakawa, 2004). It is thus not unlikely that ice bonds between grains can be characterised by different mechanical properties depending on the specific conditions of snow formation and evolution.

As further proof of DEM's good predictive capabilities, we could observe that the grain displacement fields measured for the different snow types were overall well reproduced by the simulations (Figs. 7 and 8). In particular, the model captures the radial extent of the deformation zone, i.e. of the order of 2-2.5 R. A discrepancy between the numerical and experimental profiles of radial displacement was observed for the RGlr sample. It should, however, be noted that these experimental radial displacement profiles for the RGlr sample are also those with the largest divergence compared to the prediction of the cavity expansion model (CEM) (Yu and Carter, 2002), as shown by Peinke et al. (2020). In fact, the radial profile predicted by the CEM is similar to the radial profile obtained numerically in this study.

4.2 Interpretation

4.2.1 Mechanical parameters sensitivity

The sensitivity analysis revealed a strong influence of the mechanical parameters on the simulation results. In particular, a clear dependence of the mean macroscopic force with Young's modulus E was observed, suggesting that a significant part of the sample undergoes elastic deformation, while brittle failures are confined in a region close to the tip. Note that a similar dependence to E with a cohesive contact law has been observed in DEM modelling of soil compression (De Pue et al., 2019) and snow compression (Bobillier et al., 2020). The larger cohesion and, to a smaller extent, friction angle, also tend to increase the mean force, the standard deviation and the correlation length. This can be related to the fact that increasing cohesion and friction between grains increase bond strength. It is also observed that cohesion tends to prevent bond failures, and to favour the upward movement of grains for samples with the largest initial density, such as RGlr. In contrast, increasing the friction angle enhances the bond failure rate and the downward movement of grains (Figs S12, S16, S20, S24). When sliding between grains is inhibited, a grain dragged by the tip movement will drag down surrounding grains more easily, thus enlarging the deformation zone and triggering additional bond failures. Finally, radial grain displacements and the radius of the deformation zone are mostly insensitive to the mechanical parameters, indicating that the CPT configuration and snow type mainly control these features.

4.2.2 Compaction zone development

For all snow types, the force profiles computed numerically display a 'S' shape (Figs 1, S6, S8, S10). We attribute this shape to the development of a compaction zone (CZ) in front of the tip during its progressive penetration into the numerical sample. More specifically, the first stage of the force profiles (slope increase) might be caused by the progressive cone penetration, before the cylindrical part reaches the sample. The second stage (constant slope) is attributed to the development of the CZ in front of the tip. The third stage (quasi-constant force value) suggests that a steady-state regime, with a fully-developed CZ, is reached. Depending on the snow type, the numerical results suggest that full development of the CZ occurs for 5.5 mm to 8

https://doi.org/10.5194/tc-2023-30
Preprint. Discussion started: 2 March 2023
© Author(s) 2023. CC BY 4.0 License.


mm of penetration depth. These results agree with the experimental profiles for the RG, DH and PP samples. For the RGlr sample, the experimental penetration profile did not reach the steady-state stage. Globally, we can highlight that the DEM simulations are able to reproduce fairly well the global shape of the experimental profiles, and thus to correctly capture the development of the DZ.

Nevertheless, in another experimental study, the CZ has been reported to be fully developed around 40 mm of depth penetration (Herwijnen, 2013), which is significantly deeper than the experimental and numerical results obtained in this study. A first hypothesis to explain this observation is that if our CPT force profiles reach a maximum depth of 10 mm, we might thus miss information on the full CZ development. A second hypothesis could be the differences in the experimental set-up. Indeed, Peinke et al. (2020) performed CPT on snow samples contained in cylinders of 2 cm diameter and 2 cm height, which is significantly smaller than the decimetric snow samples considered by Herwijnen (2013). Boundary effects might thus play a role. Finally, the tip geometry differs. Peinke et al. (2020) used a plain tip while Herwijnen (2013) used the original SMP tip geometry with a cone radius larger than the rod. A sensitivity analysis comparing the two geometries showed an influence over the upper 12 mm of the force profiles (Peinke, 2020). The plain tip geometry produced larger mean force and standard deviation values. This sensitivity might influence the characteristics of the CZ development.

4.2.3 Grain-tip interaction

The sensitivity analysis to the grain shape representation provides interesting insights into the interpretation of force profiles. In particular, the study highlighted that the grain shape representation could be relatively coarse (high volumetric error E_V) but still produce a force profile with an acceptable mechanical error E_M compared to a reference profile obtained for a fine grain shape representation ($E_V < 10\%$) (Fig. S1, Table S1). This is notably the case for the RG sample, as the selected grain shape representation ($R = 5$, $S = 0.3$) corresponds to a value of E_V of about 40%. Larger values of E_V often imply grain loss, as the smallest grains identified in the µCT scans cannot be represented by the DEM in this case. Despite this loss, the similarity of the force profile to the reference force profile indicates the limited contribution of these smallest grains to the macroscopic force compared to the largest grains with stronger bonds. The loss of grains and bonds might nevertheless directly affect the force fluctuations, providing a potential explanation for why the DEM model underestimates the correlation length obtained experimentally for the samples with the smallest grain sizes (RG and PP) (Figs. 5, S23).

4.2.4 Cohesive bond failure

In our DEM simulations, once broken, the cohesive interactions between grains disappear. New interaction between grains will be frictional only. Hence, we assume that bonds between grains in contact cannot reform at the time scale of the experiments. Indeed, the measurements last less than 1 s (tip velocity = 20 mm s^{-1} and sample holder height = 20 mm), while the mechanisms involved in the sintering process are generally slower (Blackford, 2007). However, subsecond sintering (millisecond process) caused by the freezing of a thin quasi-liquid layer between two grains in contact has been observed, even

https://doi.org/10.5194/tc-2023-30
Preprint. Discussion started: 2 March 2023
© Author(s) 2023. CC BY 4.0 License.


at low temperature (Szabo and Schneebeli, 2007). Including this subsecond sintering in the numerical simulations shall be considered in future works to study its role on the mechanical response of the samples.

5 Conclusion

We have evaluated a numerical model based on DEM that reproduces the mechanical behaviour of snow in the brittle regime. The DEM model is taking into account the ice properties and the snow microstructure captured by tomography. The experimental configuration of the CPT measurements conducted on different snow types by Peinke et al. (2020) has been reproduced with the DEM model. Three parameters namely, the mean force, the standard deviation of the force and the correlation length were used to quantify the similitude of the numerical and experimental profiles. The grains displacement field was computed and compared to the experimental displacement field derived from μCT scans acquired before and after the CPT.

The DEM model has demonstrated overall a good capability to simulate the mechanical responses of CPT performed in different snow types. The computed force profiles satisfactorily reproduce the main characteristics of the experimental force profiles. The results revealed that the force profiles characteristics are mainly dependent on the microstructure. A sensitivity analysis proved the dependence of the mechanical response to the mechanical parameters of the contact law. The displacement fields are also well reproduced except for the RGlr sample showing a larger extent for the numerical results. The agreement of radial displacement profiles is very good. The grains are mainly travelling downward during the CPT, although for the RGlr sample the upward movement of the grains close to the surface is not negligible. The CPT implies a complex deformation with compression zone around the apex and expansion zone close to the surface (Peinke et al., 2020). Therefore being able to reproduce the force and displacement profiles for this mechanical test constitute a strong validation of the reliability of the DEM model.

The CPT modelling via DEM model brings advantages to reproduce and interpret the snow mechanical behaviour to CPT compared to others interpretation models as it is able to take into account the high frequency fluctuations and predict the displacement field and. However, a major downside of the DEM method is the high computational cost, between 1 week to several months according to the physical and numerical parameters for the chosen CPT configuration, preventing us from exploring all the range of mechanical parameters chosen for all the snow types. Besides, the DEM model could be improved by adding time-dependent parameters in the contact laws to take into account the sintering process.

The developed DEM model constitutes a versatile approach that can be applied to various materials and configurations. In particular, the DEM model can be used to study the interaction between the tip and the grains of the numerical sample to better interpret the CPT force profiles. Pertinent macro and micromechanical parameters could be derived to characterise the microstructure properties from the CPT force signal solely. Especially the validity of the assumptions made by the HPP-NHPP method as well as the influence of the CZ development will be tested. Critical structural parameters driving the mechanical

https://doi.org/10.5194/tc-2023-30
Preprint. Discussion started: 2 March 2023
© Author(s) 2023. CC BY 4.0 License.


behaviour, could be identified and a parameterization developed in order to include the effect of snow microstructure in macroscale numerical models studying snowpack and avalanches.

Code availability

Codes can be provided by the corresponding authors upon request.

Data availability

All data can be provided by the corresponding authors upon request.

Author contribution

CH, PH and GC developed the numerical model, CH performed simulations and evaluated the numerical model, IP, PH, GC, JR designed experiment, IP acquired experimental data, IP processed and analysed experimentation measurements, CH analysed and interpreted numerical results, CH wrote the manuscript draft, PH and GC reviewed and edited the manuscript.

Competing interests

GC is a member of the editorial board of The Cryosphere. The peer-review process was guided by an independent editor, and the authors have also no other competing interests to declare.

Acknowledgements

This work benefited from financial supports from the Centre National de la Recherche Scientifique (CNRS), the Centre National de la Recherche Météorologique, the Agence Nationale de la Recherche (Project ANR MiMESis-3D ANR-19-CE01-0009).

References

Bartelt, P., and M. Lehning.: A physical SNOWPACK model for the Swiss avalanche warning: Part I—Numerical model, Cold Reg. Sci.Technol.,35(3), 123–145, doi: 10.1016/S0165-232X(02)00074-5, 2002.

Bishop, R. F., Hill, R., and F Mott, N.: The theory of indentation hardness tests, Proc. Phys. Soc. 57:321, doi: 10.1088/0959-5309/57/3/301, 1945.

© Author(s) 2023. CC BY 4.0 License.


595 Blackford, J. R.: Sintering and microstructure of ice: a review, J. Phys. D. Appl. Phys. 40, R355–R385, doi: 10.1088/0022-3727/40/21/R02, 2007.

Bobillier, G., Bergfeld, B., Capelli, A., Dual, J., Gaume, J., Herwijnen, A., and Schweizer, J.: Micromechanical modeling of snow failure, The Cryosphere, 14, 39–49, doi:10.5194/tc-14-39-2020, 2020.

Bobillier, G., Bergfeld, B., Dual, J., Gaume, J., Herwijnen, A., and Schweizer, J.: Micro-mechanical insights into the dynamics
600 of crack propagation in snow fracture experiments, Sci Rep 11, 11711, doi :10.1038/s41598-021-90910-3, 2021.

Bolton, M. D., Gui, M. W., and Phillips, R.: "Review of miniature soil probes for model tests," in Proceedings of the 11th Southeast Asian Geotechnical Conference (Singapore), 85–90, 1993.

Brun, E., David, P., Sudul, M., and Brunot, G.: A numerical model to simulate snow-cover stratigraphy for operational avalanche forecasting, J. Glaciol., 38(128), 13–22, doi: 10.3189/S0022143000009552, 1992.

605 Calonne, N., F. Flin, C. Geindreau, B. Lesaffre and S. Rolland du Roscoat: Study of a temperature gradient metamorphism of snow from 3-D images: time evolution of microstructures, physical properties and their associated anisotropy, The Cryosphere, 8, 2255-2274, doi: 10.5194/tc-8-2255-2014, 2014.

Calonne, N., F. Flin, B. Lesaffre, A. Dufour, J. Roulle, P. Puglièse, A. Philip, F. Lahoucine, C. Geindreau, J.-M. Panel, S. Rolland du Roscoat and P. Charrier, CellDyM : a room temperature operating cryogenic cell for the dynamic monitoring of
610 snow metamorphism by time-lapse X-ray microtomography, Geophys. Res. Lett., 42, doi: 10.1002/2015GL06354, 2015.

Coléou, C., B. Lesaffre, J.-B. Brzoska,W. Ludwig and E. Boller: Three dimensional snow images by X-ray microtomography, Ann. Glaciol., 32, 75-81, doi : 10.3189/172756401781819418, 2001.

Coeurjolly, D. and Montanvert, A.: Descripteurs de forme et moments géométriques. Géométrie discrète et images numériques, Hermès, 2007.

615 De Pue, J., Di Emidio, G., Verastegui Flores, R. D., Bezuijen, A., and Cornelis, W. M.: Calibration of DEM material parameters to stimulate stress-strain behaviour of unsaturated soils during uniaxial compression, Soil and Tillage Research, 194, 104303, doi: 10.1016/j.still.2019.104303, 2019.

Dowd, T. and Brown, R.L.: A new instrument for determining strength profiles in snow cover, Journal of Glaciology, 32(111): 299–301, doi: 10.3189/S0022143000015628, 1986.

620 Fierz, C., Armstrong, R. L., Durand, Y., Etchevers, P., Greene, E., and McClung, D. M.: "The international classification for seasonal snow on the ground," in Tech. Doc. Hydrol. 83 Paris: UNESCO, 2009.

Fish, A. M. and Zaretsky, Y. K.: Ice strength as a function of hydrostatic pressure and temperature, CRREL report, 38207814, 1997.

Floyer, J.A., and Jamieson, J.B. Rate-effect experiments on round-tipped penetrometer insertion into uniform snow, Journal
625 of Glaciology, 56(198): 664–672. doi:10.3189/002214310793146322, 2010.

Freitag, J., Wilhelms, F. and Kipfstuhl, S.: Microstructure dependent densification of polar firn derived from X-ray microtomography, J. Glaciol., 50(169), 243–250, doi: 10.3189/172756504781830123, 2004.

© Author(s) 2023. CC BY 4.0 License.


Gammon, P. H., Kiefte; H., Clouter, M. J. and Denner, W. W.: Elastic constants of artificial and natural ice samples by Brillouin spectroscopy, Journal of Glaciology, 29(103), 433-460, doi: 10.3189/S0022143000030355, 1983.

Gaume, J., van Herwijnen, A., Chambon, G., Birkeland, K. W., and Schweizer, J.: Modeling of crack propagation in weak snowpack layers using the discrete element method, The Cryosphere, 9, 1915–1932. doi: 10.5194/tc-9-1915-2015, 2015.

Gaume, J., van Herwijnen, A., Chambon, G.,Wever, N., and Schweizer, J.: Snow fracture in relation to slab avalanche release: Critical state for the onset of crack propagation, The Cryosphere, 11(1), 217–228, doi: 10.5194/tc-11-217-2017, 2017.

Gubler, H. U.: On the ramsonde hardness equation, IAHS-AISH Publ. 114, 110–121, 1975.

Gubler, H. U.: Determination of the mean number of bonds per snow grain and of the dependence of the tensile strength of snow on stereological parameters, J. Glaciol. 20, 329–341, doi: 10.3189/S0022143000013885, 1978.

Hagenmuller, P., Chambon, G., Lesaffre, B., Flin, F., and Naaim, M.: Energy-based binary segmentation of snow microtomographic images, J. Glaciol. 59 (217), 859–873, doi: 10.3189/2013JoG13J035, 2013.

Hagenmuller, P., Calonne, N., Chambon, G., Flin, F., Geindreau, C., and Naaim, M.: Characterization of the snow microstructural bonding system through the minimum cut density, Cold Reg. Sci. Technol. 108, 72–79, doi: 10.1016/j.coldregions.2014.09.002, 2014.

Hagenmuller, P., Chambon, G., Flin, F., Morin, S., and Naaim, M.: Snow as a granular material: assessment of a new grain segmentation algorithm, Gran. Matter 16 (4), 421–432, doi: 10.1007/s10035-014-0503-7, 2014.

Hagenmuller, P., Chambon, G., and Naaim, M.: Microstructure-based modeling of snow mechanics: A discrete element approach, Cryosphere, 9(5), 1969–1982, doi: 10.5194/tc-9-1969-2015, 2015.

Hansen, A. C. and Brown, R. L.: An internal state variable approach to constitutive theories for granular materials with snow as an example, Mech. Mater., 7, 109–119, doi: 10.1016/0167-6636(88)90009-9, 1988.

Heggli, M., B. Köchle, M. Matzl, B. R. Pinzer, F. Riche, S. Steiner, D. Steinfeld, and M. Schneebeli: Measuring snow in 3-D using X-ray tomography: Assessment of visualization techniques, Ann. Glaciol., 52(58), 231–236, doi:10.3189/172756411797252202, 2011.

Herwijnen, A. V.: Experimental analysis of snow micropenetrometer (SMP) cone penetration in homogeneous snow layers, Can. Geotech. J. 50, 1044–1054. doi: 10.1139/cgj-2012-0336, 2013.

Jamieson, J. B., and Johnston, C. D.: Snowpack characteristics associated with avalanche accidents, Canadian Geotechnical Journal, 29(5), 862–866, doi: 10.1139/t92-093, 1992.

Johnson, J., and Schneebeli, M.: Characterizing the microstructural and microchemical properties of snow, Cold Reg. Sci. Technol. 30, 91–100. doi: 10.1016/S0165232X(99)00013-0, 1999.

Johnson, J. B. and Hopkins, M. A.: Identifying microstructural deformation mechanisms in snow using discrete-element modeling, J. Glaciol., 51, 432–442. doi: 10.3189/172756505781829188, 2005.

Kozak, M. C., Elder, K., Birkeland, K., and Chapman, P.: Variability of snow layer hardness by aspect and prediction using meteorological factors, Cold Regions Science and Technology, 37(3): 357–371. doi:10.1016/S0165-232X(03)00076-4, 2003.

© Author(s) 2023. CC BY 4.0 License.


Lunne, T., Robertson, P. K., and Powell, J. J. M.: Cone penetration testing in geotechnical practice. Blackie Academic, EF Spon/Routledge, New York, 1997.

LeBaron, A., Miller, D., and van Herwijnen, A.: Measurements of the deformation zone around a split-axis snow micropenetrometer tip, Cold Reg. Sci. Technol. 97, 90–96. doi: 10.1016/j.coldregions.2013.10.008, 2014.

Lowe, H., and van Herwijnen, A.: A Poisson shot noise model for micropenetration of snow, Cold Regions Science and Technology, 70: 62–70. doi: 10.1016/j.coldregions.2011.09.001, 2012.

McCallum, A.: A brief introduction to cone penetration testing (CPT) in frozen geomaterials, Ann. Glaciol. 55, 7–14. doi: 10.3189/2014 AoG68A005, 2014.

Mackenzie, R., and Payten, W.: A portable, variable-speed, penetrometer for snow pit evaluation, In Proceedings of the 2002 International Snow Science Workshop, Penticton, B.C. pp. 294–300, 2002.

Maeno, N. and Arakawa, M.: Adhesion shear theory of ice friction at low sliding velocities, combined with ice sintering, Journal of Applied Physics, 95(1), 134-139, doi: 10.1063/1.1633654, 2004.

Marshall, H.P., and Johnson, J.B.: Accurate inversion of high-resolution snow penetrometer signals for microstructural and micromechanical properties, Journal of Geophysical Research: Earth Surface, 114(F4): F04016. doi: 10.1029/2009JF001269, 2009.

Mede, T., Chambon, G., Hagenmuller, P., and Nicot, F.: A medial axis based method for irregular grain shape representation in DEM simulations, Granular Matter, 20(1), 1-11, doi: 10.1007/s10035-017-0785-7, 2018a.

Mede, T., Chambon, G., Hagenmuller, P., and Nicot, F.: Snow failure modes under mixed loading, Geophys. Res. Lett. 45 (24), 13–351, doi: 10.1029/2018GL080637, 2018b.

Mede, T., Chambon, G., Nicot, F., and Hagenmuller, P.: Micromechanical investigation of snow failure under mixed-mode loading, International Journal of Solids and Structures, 199, 95–108. doi:10.1016/j.ijsolstr.2020.04.020, 2020.

Montagnat, M., Löwe, H., Calonne, N., Schneebeli, M., Matzl, M. and Jaggi, M.: On the birth of structural and crystallographic fabric signals in polar snow: A case study from the EastGRIP snowpack, Frontiers in Earth Science, 8:365. doi:10.3389/feart.2020.00365, 2020.

Narita, H.: An experimental study on tensile fracture of snow, Contribut. Inst. Low Temperat. Sci. A32, 1–37, 1983.

Peinke, I., Hagenmuller, P., Chambon, G., and Roulle, J.: Investigation of snow sintering at microstructural scale from micro-penetration tests, Cold Reg. Sci. Technol. 162, 43–55. doi: 10.1016/j.coldregions.2019.03.018, 2019.

Peinke, I., Hagenmuller, P., Andò, E., Chambon, G., Flin, F. and Roulle, J.: Experimental Study of Cone Penetration in Snow Using X-Ray Tomography, Front. Earth Sci. 8:63. doi: 10.3389/feart.2020.00063, 2020.

Proksch, M., Löwe, H., and Schneebeli, M.: Density, specific surface area, and correlation length of snow measured by high-resolution penetrometry, J. Geophys. Res. Earth Surf. 120, 346–362. doi: 10.1002/2014JF003266, 2015.

Reuter, B., Schweizer, J., and van Herwijnen, A.: A process-based approach to estimate point snow instability, Cryosphere, 9, 837–847. doi: 10.5194/tc-9-837-2015, 2015.

© Author(s) 2023. CC BY 4.0 License.


Reuter, B., Proksch, M., Löwe, H., Van Herwijnen, A., and Schweizer, J.: Comparing measurements of snow mechanical properties relevant for slab avalanche release, J. Glaciol. 65, 55–67. doi: 10.1017/jog.2018.93, 2019.

Ruiz, S., Straub, I., Schymanski, S. J., and Or, D.: Experimental evaluation of earthworm and plant root soil penetration-cavity expansion models using cone penetrometer analogs, Vadose Zone J. 15, 1–14. doi: 10.2136/vzj2015. 09.0126, 2016.

Ruiz, S., Capelli, A., van Herwijnen, A., Schneebeli, M., and Or, D.: Continuum cavity expansion and discrete micromechanical models for inferring macroscopic snow mechanical properties fromcone penetration data, Geophys. Res. Lett. 44, 8377–8386. doi: 10.1002/2017GL074063, 2017.

Shapiro, L.H., Johnson, J. B., Sturm, M., and Blaisdell, G. L.: Snow mechanics: review of the state of knowledge and applications, CRREL Rep. 97-3, 1997.

Schaap, L. H. J. and Fohn, P. M. B.: Cone penetration testing in snow, Canadian Geotechnical Journal 24(3):335-341. doi:10.1139/t87-044, 2011.

Schneebeli, M.: Numerical simulation of elastic stress in the microstructure of snow, Annals of Glaciology, 38. doi: 10.3189/172756404781815284, 2004.

Schneebeli, M., and Johnson, J. B.: A constant-speed penetrometer for high resolution snow stratigraphy, Annals of Glaciology, 26: 107–111, doi: 10.3189/1998AoG26-1-107-111, 1998.

Schneebeli, M., and Sokratov. S. A.: Tomography of temperature gradient metamorphism of snow and associated changes in heat conductivity, Hydrol. Process., 18(18), 3655–3665, doi: 10.1002/hyp.5800, 2004.

Schulson, E. M. and Duval, P.: Creep and Fracture of Ice, Cambridge University Press, 2009.

Schweizer, J., Jamieson, J. B., and Schneebeli, M.: Snow avalanche formation, Rev. Geophys., 41(4), 1016. doi:10.1029/2002RG000123, 2003.

Šmilauer, V., Catalano, E., Chareyre, B., Dorofeenko, S., Duriez, J., Gladky, A., Kozicki, J., Modenese, C., Scholtès, L., Sibille, L., Stransky, J., and Thoeni, K.: Yade reference documentation. In V. Šmilauer (Ed.), Yade Documentation (Vol. 474). Retrieved from http://yadedem.org/doc, 2010/

Szabo, D. and Schneebeli, M.: Subsecond sintering of ice, Applied Physics Letters, 90, 151916, doi: 10.1063/1.2721391, 2007.

Thorsteinsson, T.: An analytical approach to deformation of anisotropic ice-crystal aggregates, Journal of Glaciologiy, 47 (158), 507-516, doi; 10.3189/172756501781832124, 2001.

Vionnet, V., Brun, E., Morin, S., Boone, A., Faroux, S., Le Moigne, P., Martin, E. and Willemet, J.-M.: The detailed snowpack scheme Crocus and its implementation in SURFEX v7.2, Geosci. Model Dev., 5, 773-791. doi: 10.5194/gmd-5-773-2012, 2012.

Wautier, A., Geindreau, C., and Flin, F.: Linking snow microstructure to its macroscopic elastic stiffness tensor: A numerical homogenization method and its application to 3-D images from x-ray tomography, Geophysical Research Letters, 42, 8031–8041. https://doi.org/10.1002/2015GL065227, 2015.

Yu, H. S., and Carter, J.: Rigorous similarity solutions for cavity expansion in cohesive-frictional soils, Int. J. Geomech., 2, 233–258. doi:10.1061/(ASCE)1532-3641(2002)2:2(233), 2002.